Journal Pre-proof

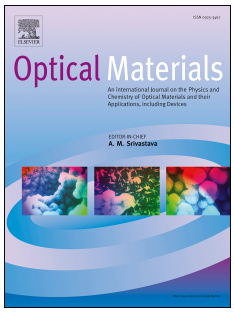

Growth, spectroscopy and 2 μm laser operation of monoclinic Tm^{3+}:$ZnWO_4$ crystal

Ghassen Zin Elabedine, Kirill Subbotin, Pavel Loiko, Zhongben Pan, Kirill Eremeev, Yulia Zimina, Yana Didenko, Sergei Pavlov, Anatoly Titov, Elena Dunina, Liudmila Fomicheva, Aleksey Kornienko, Alain Braud, Rosa Maria Solé, Magdalena Aguiló, Francesc Díaz, Weidong Chen, Pavel Volkov, Valentin Petrov, Xavier Mateos

PII: S0925-3467(24)01222-9

DOI: https://doi.org/10.1016/j.optmat.2024.116039

Reference: OPTMAT 116039

To appear in: *Optical Materials*

Received Date: 23 May 2024

Revised Date: 31 July 2024

Accepted Date: 30 August 2024

Please cite this article as: G. Zin Elabedine, K. Subbotin, P. Loiko, Z. Pan, K. Eremeev, Y. Zimina, Y. Didenko, S. Pavlov, A. Titov, E. Dunina, L. Fomicheva, A. Kornienko, A. Braud, R.M. Solé, M. Aguiló, F. Díaz, W. Chen, P. Volkov, V. Petrov, X. Mateos, Growth, spectroscopy and 2 μm laser operation of monoclinic Tm^{3+}:$ZnWO_4$ crystal, *Optical Materials*, https://doi.org/10.1016/j.optmat.2024.116039.

Growth, spectroscopy and 2 μm laser operation of monoclinic Tm^{3+}:$ZnWO_4$ crystal

Ghassen Zin Elabedine,[1] Kirill Subbotin,[2,3] Pavel Loiko,[4] Zhongben Pan,[5] Kirill Eremeev,[4] Yulia Zimina,[2,3] Yana Didenko,[2] Sergei Pavlov,[2] Anatoly Titov,[2] Elena Dunina,[6] Liudmila Fomicheva,[7] Aleksey Kornienko,[6] Alain Braud,[4] Rosa Maria Solé,[1] Magdalena Aguiló,[1] Francesc Díaz,[1] Weidong Chen,[8,9] Pavel Volkov,[10] Valentin Petrov,[8] and Xavier Mateos[1,#,*]

[1]*Universitat Rovira i Virgili (URV), Física i Cristal·lografia de Materials (FiCMA),43007 Tarragona, Spain.* [#]*Serra Húnter Fellow, Spain*
[2]*Prokhorov General Physics Institute, Russian Academy of Sciences, 38 Vavilova St., 119991 Moscow, Russia*
[3]*Mendeleev University of Chemical Technology of Russia, 9 Miusskaya Sq., 125047 Moscow, Russia*
[4]*Centre de Recherche sur les Ions, les Matériaux et la Photonique (CIMAP), UMR 6252 CEA-CNRS-ENSICAEN, Université de Caen Normandie, 6 Boulevard Maréchal Juin, 14050 Caen Cedex 4, France*
[5]*School of Information Science and Engineering, Shandong University, Qingdao 266237, China*
[6]*Vitebsk State Technological University, 72 Moskovskaya Ave., 210035 Vitebsk, Belarus*
[7]*BIP - University of Law and Social-Information Technologies, Department of IT and Mathematics, 3 Korol St., 220004 Minsk, Belarus*
[8]*Max Born Institute for Nonlinear Optics and Short Pulse Spectroscopy, Max-Born-Str. 2a, 12489 Berlin, Germany*
[9]*Fujian Institute of Research on the Structure of Matter, Chinese Academy of Sciences, Fuzhou, 350002 Fujian, China*
[10]*NRC "Kurchatov Institute", Akademik Kurchatov Sq. 1, 123098 Moscow, Russia*
**Corresponding author, e-mail: xavier.mateos@urv.cat*

Abstract: We report on the crystal growth, polarized spectroscopy, and laser operation of monoclinic Tm^{3+}, Na^+(Li^+) codoped zinc monotungstate ($ZnWO_4$) crystals. The Li^+ codoping with an optimized Tm/Li ratio enables almost complete local charge compensation leading to better crystal quality, higher Tm segregation coefficient, and longer luminescence lifetime and ultimately the demonstration of laser operation. The modified Judd-Ofelt theory was employed to calculate the Tm^{3+} transition probabilities yielding a radiative lifetime of the $^3F_4$ state of 2.59 ms. The corresponding intensity parameters are Ω_2 = 5.194, Ω_4 = 0.658, Ω_6 = 0.471 [10^{-20} cm^2] and α = 0.110 [10^{-4} cm]. Tm,Li:$ZnWO_4$ features strongly polarized emission spectra extending beyond 2 μm owing to a large total Stark splitting of the ground-state, $\Delta E(^3H_6)$ = 644 cm^{-1}. The stimulated-emission cross-section in this spectral range reaches 0.47×10^{-20} cm^2 at 2015 nm for light polarization $\boldsymbol{E} \parallel N_p$. The continuous-wave Tm,Li:$ZnWO_4$ laser generated 282 mW at 1.98 μm with a slope efficiency of 14.7%, and laser emission at 2.03 μm was also achieved.

Keywords: laser materials; thulium ions; optical spectroscopy; luminescence; Judd-Ofelt theory; solid-state lasers.

1. Introduction

Monoclinic divalent metal monotungstates with chemical formula $M^{2+}WO_4$ (where M stands for Mg, Zn, Cd, Mn, etc.) are appealing optical materials. They were first recognized as efficient scintillators [1] to search for rare nuclear and sub-nuclear processes such as double beta decay, dark matter particles, or to investigate rare α- and β-decays. More recently, they attracted attention for photonics applications, notably as Raman shifters [2,3] and laser gain media [4–7]. The $M^{2+}WO_4$ crystals present a single crystallographic site for M^{2+} cations which can easily accommodate various transition-metals and, in particular, Cr^{3+} ions [8]. Although the solubility of trivalent rare-earth ions (RE^{3+}) in $M^{2+}WO_4$ crystals is relatively low due to the difference in the ionic radii and charge of the dopant and host-forming cations, RE^{3+}-doped $M^{2+}WO_4$ crystals exhibit attractive spectroscopic properties motivating their studies.

As laser host matrices, $M^{2+}WO_4$ crystals and, in particular, $MgWO_4$ and $ZnWO_4$, combine good thermo-mechanical properties (high thermal conductivity [9], weak anisotropy of the thermal expansion [7], and high thermal fracture limit [10]) with intriguing spectroscopic features of the dopant RE^{3+} ions such as Yb^{3+} or Tm^{3+} [4,6,11]. In particular, they offer i) intense and strongly polarized absorption and emission spectral bands which is a prerequisite for linearly polarized emission; ii) strong crystal fields leading to large total Stark splitting of the ground states resulting in broad emission bands and low-threshold laser behavior [4–6]; and iii) remarkable spectral line broadening arising from a combination of strong electron-phonon interaction and inhomogeneous line broadening related to the $RE^{3+} \rightarrow Zn^{2+}$ substitution requiring local charge compensation.

Trivalent rare-earth ions doped into crystalline matrices give rise to various laser lines falling into the visible, near and mid-infrared spectral ranges. Among the rare-earth dopants, thulium (Tm^{3+}) ions exhibit superior spectral features in $M^{2+}WO_4$ crystals compared to other oxide host crystals in terms of combination of a large Stark splitting of their multiplets (being record-high among other tungstate compounds) and strongly polarized emission spectra extending beyond 2 μm, as proven for the case of $MgWO_4$ [6]. The latter is of key importance for generating femtosecond pulses at 2 μm avoiding the structured absorption of water vapors in the air at ~1.9 μm. Tm lasers emitting in the relatively "eye-safe" spectral range of 2 μm find applications in range-finding (LIDAR), wind mapping [12], medicine, and they are relevant as pump sources of 2.1-μm Holmium (Ho) lasers [13] and optical parametric amplifiers for the mid-infrared spectral range [14].

Tm:$MgWO_4$ crystals showed a great promise for power-scalable multi-Watt diode-pumped continuous-wave (CW) lasers emitting at 2 μm, achieving, e.g., 3.09 W at 2.03 μm with a slope efficiency of 50% [15]. Broadband wavelength tuning of a Tm:$MgWO_4$ laser across the wavelength range of 1897 - 2062 nm, and operation at 2.09 μm relying on the vibronic (electron-phonon coupling) mechanism were also demonstrated [6]. Even more important, the first sub-100 fs pulses from a solid-state oscillator at 2 μm were generated employing a Tm:$MgWO_4$ crystal [16]. Using a graphene saturable absorber, the passively mode-locked laser delivered 86 fs pulses

at 2017 nm at a repetition rate of 76 MHz. Even shorter pulses (76 fs at 2037 nm) were achieved via single walled carbon nanotube assisted Kerr-lens mode-locking [17].

Despite the encouraging results achieved with Tm:$MgWO_4$ crystals in terms of their 2-μm laser performance, further laser development was mostly mitigated by the material considerations, namely i) incongruent melting of $MgWO_4$ imposing complicated growth by the Top-Seeded Solution method (from the flux) [18] and ii) very low segregation coefficients of Tm^{3+} ions [18] limiting the pump absorption efficiency. Moderate to high doping would also be required to benefit from the cross-relaxation mechanism between adjacent Tm^{3+} ions boosting the pump quantum efficiency.

Considering these constraints, we turned our attention to the zinc monotungstate, $ZnWO_4$. It melts congruently at 1213 °C and can be grown by the Czochralski (Cz) method resulting in large volume crystal boules of high optical quality [11,19]. Moreover, $ZnWO_4$ offers higher solubility of rare earths. Cz growth of $ZnWO_4$ crystals with different RE^{3+} dopants including Tm^{3+} was reported in [11,20–22] but the spectroscopic data were incomplete (in particular, the polarization dependence was not addressed) and no conclusive statement about the laser potential could be made.

Recently, we performed a systematic study of Yb^{3+},Li^+ codoped $ZnWO_4$ crystals revisiting their structure, anisotropic optical and polarized spectroscopic properties [5,11]. It was shown that the crystal-field splitting of Yb^{3+} multiplets in $ZnWO_4$ is larger than that for $MgWO_4$ which is an attractive feature in the search of novel broadly emitting laser materials. Moreover, we highlighted the role of local charge compensation by Li^+. This aspect was further studied in [23] regarding the mechanical properties of RE^{3+}-doped $ZnWO_4$ crystals.

In the present work, we report on a comprehensive study of $ZnWO_4$ crystals codoped with laser-active Tm^{3+} ions and univalent alkali metal cations (Na^+ or Li^+) acting as charge compensators, with the goal of developing novel broadband emitting laser materials for ultrafast lasers operating slightly above 2 μm. The novelty of this work consists of i) the first polarization-resolved study of spectroscopic properties of Tm^{3+} ions in zinc monotungstate, ii) the first report on the crystal-field splitting for Tm^{3+} ions in this crystal by low-temperature spectroscopy, iii) the first study of the effect of charge compensators on the properties of Tm^{3+}-doped $ZnWO_4$, as well as iv) the first laser operation of Tm^{3+},Li^+:$ZnWO_4$ crystals.

2. Crystal growth

Two Tm^{3+}-doped $ZnWO_4$ crystals containing different charge compensators (Na^+ or Li^+ ions) were grown using the Czochralski (Cz) method with distinct parameters and conditions. The crystal codoped with Tm^{3+},Na^+ ions was grown using argon atmosphere in an iridium crucible. An automatic system was employed to control the boule diameter. The starting materials, Na_2CO_3 (purity: 4N), ZnO, WO_3 and Tm_2O_3 (purity: 5N), were first weighed according to the chemical formula $Na_{0.05}Tm_{0.05}Zn_{0.9}WO_4$, i.e., the starting Tm^{3+} and Na^+ doping levels were 5 at.% (with respect to Zn^{2+}). Then they were mixed, ground and heated at 650 °C for 10 h to decompose

Na_2CO_3 in a platinum crucible. After the crucible was cooled down to room temperature, the mixture was pressed into pellets and reheated at 1000 ℃ for 15 h to form the Tm,Na:$ZnWO_4$ polycrystalline material through a solid-state reaction:

$1.8ZnO + 2WO_3 + 0.05Tm_2O_3 + 0.05Na_2CO_3 \rightarrow 2Na_{0.05}Tm_{0.05}Zn_{0.9}WO_4 + 0.05CO_2\uparrow$.

The synthesized polycrystalline material was placed in an iridium crucible and melted by an intermediate-frequency heater. To remove bubbles from the melt and to avoid the formation of polycrystals during the growth process, a homogenization of the melt at a temperature of 30–50 ℃ above the melting point is required. The temperature was held at this point for 2-3 h, and then decreased down to the melting point. A seed cut from an undoped crystal and oriented along the [001] direction was used. The pulling rate varied from 0.5 to 1.0 mm/h, and the crystal rotation speed was kept at 8 to 15 revolutions per minute (r.p.m.). After the growth was completed, the crystal was removed from the melt and slowly cooled down to room temperature at a stepped rate of 15 to 25 ℃/h.

The obtained boule of Tm,Na:$ZnWO_4$ had dimensions of ∅25×45 mm^3. The boule had a cylindrical shape with uniform diameter without developed natural faceting. It contained no cracks or inclusions. The as-grown crystal had a nearly black coloration due to the presence of color centers formed during the growth under oxygen deficient conditions [11]. After annealing in air for several days, the coloration of the crystal changed to wine-brown, and the transparency was improved as seen in Fig. 1(a).

By using X-ray fluorescence, the actual Tm^{3+} doping level in the crystal was determined to be 1.14 at.% (ion density: $N_{Tm} = 1.72\times10^{20}$ at/cm^3) resulting in a segregation coefficient $K_{Tm} = C_{crystal}/C_{melt}$ of 0.228. This relatively low value is mostly due to the large difference between the ionic radii and charge of Tm^{3+} and Zn^{2+} (see below). We were unable to quantify the actual content of Na^+ by this method.

The crystal codoped with Tm^{3+},Li^+ ions was also grown by the Cz method at the “Kristall-2” growth machine (USSR) in air using a Pt crucible with a diameter / height of ∅40 mm / 40 mm, respectively, and a [001] oriented seed cut from an undoped $ZnWO_4$ single crystal. The raw materials were ZnO (purity: 5N), WO_3 (5N), Tm_2O_3 (4N) and Li_2CO_3 (4N). The Tm^{3+} / Li^+ content in the initial melt was optimized to be 4 at.% and 8 at.%, respectively, with respect to Zn^{2+}. This high content of Li^+ was intentionally selected to reach nearly complete charge compensation. Prior to melting, the blend of the initial chemicals was thoroughly mixed and then calcined at 700 °C during 5 hours for solid-phase synthesis.

The pulling / rotation rates were 1 mm/h and 6 r.p.m., respectively. After the growth was completed, the crystal was removed from the melt and slowly cooled to room temperature at a rate of 8 °C/h to reduce the risk of cracking. The crystal was additionally annealed in air at 800 °C for 2 weeks. A photograph of the as-grown crystal is provided in Fig. 1(b). It had a cylindrical shape with a length of 30 mm and a slightly varying diameter of 10-13 mm. The as-grown boule of high

optical quality had much weaker coloration than that codoped with Tm^{3+},Na^{+}. After annealing, it was almost completely removed resulting in a light-brown hue.

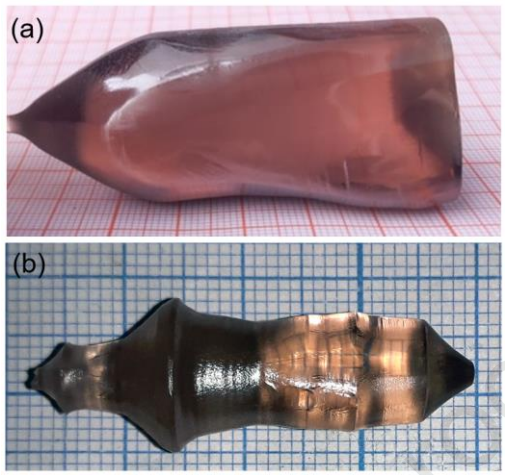

Figure 1. Photographs of the as-grown crystal boules: (a) Tm,Na:$ZnWO_4$ after annealing; (b) Tm,Li:$ZnWO_4$ before annealing. The growth direction is [001].

The actual concentrations of Tm^{3+} and Li^{+} in the Tm,Li:$ZnWO_4$ crystal were measured by Atomic Emission Spectrometry with Inductively Coupled Plasma (AES ICP) at iCAP 6300 duo spectrometer (Thermo Scientific), using a set of multi-element standards (High-Purity Standards). For the probe fabrication, the crystalline samples were ground into powders and dissolved in orthophosphoric acid (Suprapur, Merck), at temperatures up to 400 °C. The actual Tm^{3+} doping level for this second crystal appeared to be 1.59 at.% (N_{Tm} = 2.4×10^{20} at/cm^3) and the segregation coefficient K_{Tm} is as high as 0.40 owing to the positive effect of Li^{+} codoping. Meanwhile, the actual Li^{+} content in the crystal was measured to be 1.65 at. %, and the segregation coefficient K_{Li} was only 0.21. Note that the optimized Tm^{3+}/Li^{+} concentration ratio in the charge provides almost equimolar actual concentrations of these ions in the crystal, and, consequently, almost complete mutual charge compensation of heterovalent $Tm^{3+} \rightarrow Zn^{2+}$ and $Li^{+} \rightarrow Zn^{2+}$ substitution.

3. Crystal structure

The crystal structure of Tm^{3+},Li^{+}:$ZnWO_4$ was refined by the Rietveld method based on X-ray powder diffraction (XRD). We used a Bruker-AXS D8-Advance diffractometer equipped with a vertical θ-θ goniometer, Cu Kα radiation, and a LynxEye-XE-T position-sensitive detector with an opening angle of 2.94°. The data acquisition spanned the 2θ range of 10 to 80°, with a step size of 0.02° and a step time of 2 s. The powder XRD pattern is shown in Fig. 2(a), in comparison with a reference standard, pure $ZnWO_4$ (ICDS card No. 084540). The analysis revealed a consistent alignment of all diffraction peaks with the reference standard, with no additional peaks indicative of impurities, thereby affirming the phase purity of the crystal. The Rietveld method was

implemented using the Topas V6 software, see Fig. 2(b) presenting the observed, calculated and residual patterns. The undoped $ZnWO_4$ crystal structure [24] served as the initial model for the structure refinement.

The refinement indicates that Tm^{3+}, Li^+:$ZnWO_4$ belongs to the monoclinic class adopting the C_{2h}^4 - *P*2/*c* space group (No. 13) and the 2/*m* point group, with a general multiplicity Z of 2. The lattice constants of the crystal are a = 4.699(0) Å, b = 5.720(7) Å, c = 4.930(5) Å, and the monoclinic angle $\beta = \boldsymbol{a} \wedge \boldsymbol{c}$ = 90.686°, slightly exceeding those of an undoped $ZnWO_4$ crystal (a = 4.692 Å, b = 5.721 Å, c = 4.928 Å, and β = 90.632°) [24]. The calculated unit-cell volume V is 132.5(3)Å^3, slightly larger than that for undoped $ZnWO_4$ (V = 132.3 Å^3), confirming the partial substitution of Zn^{2+} by Tm^{3+} and Li^+. Indeed, the ionic radii of Tm^{3+} and Li^+ (0.88 Å and 0.76 Å, respectively, for VI-fold oxygen coordination) are larger than that of Zn^{2+} (0.74 Å). The calculated crystal density ρ_{calc} is 7.836 g/cm^3. The Rietveld refinement data are summarized in Table 1. The reliability factors are R_p = 5.84%, R_{wp}= 7.60%, and R_{exp}=4.54%, so that the reduced chi-squared value $\chi^2 = (R_{wp}/R_{exp})^2$ is 1.67, indicating the convergence of the fit.

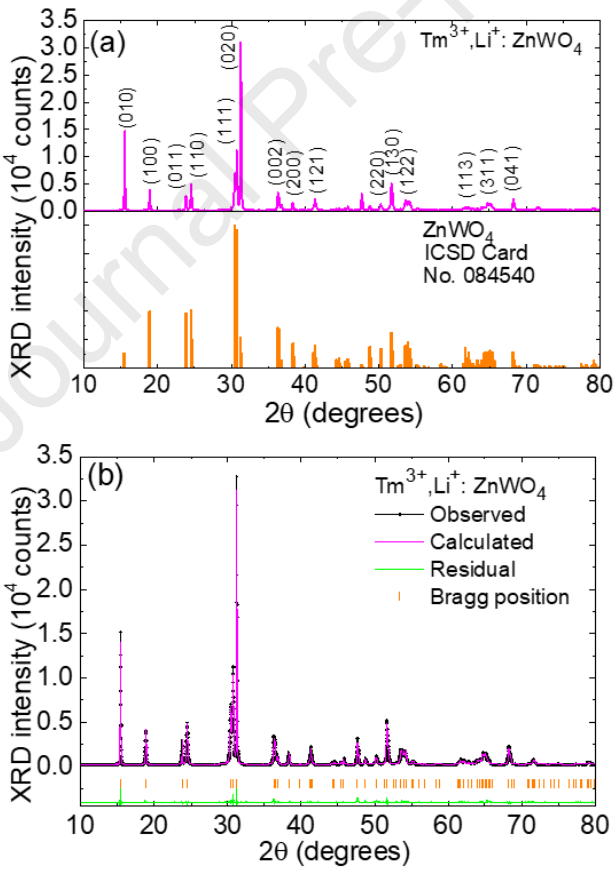

Figure 2. X-ray powder diffraction (XRD) study of Tm^{3+},Li^+:$ZnWO_4$: (a) XRD pattern, *vertical bars* – theoretical pattern for undoped $ZnWO_4$, (*hkl*) – Miller's indices; (b) Rietveld structure refinement: experimental (*black*), calculated (*magenta*) and differential (*green*) XRD profiles, *vertical dashes* mark the Bragg reflections.

Table 1. Parameters of the Rietveld refinement of the Tm^{3+},Li^{+}:$ZnWO_4$ crystal.

Data	Tm^{3+}, Li^{+}:$ZnWO_4$
Crystal system	Monoclinic
Space group (IT number)	*P*2/*c* (13)
Laue class	2/*m*
Calculated density (g/cm^3)	7.836
Lattice constant *a*, *b*, *c*(Å)	4.699(0), 5.720(7), 4.930(5)
α, *β*, *γ* (deg.)	90, 90.686, 90
Unit-cell volume (Å^3)	132.5(3)
2θ range (deg.)	10 - 80
2θ step	0.02
Radiation	Cu-Kα1 (λ = 1.5418 Å)
No. of reflections	85
Refinement software	Topas V6
Reliability factors	R_p = 5.84, R_{wp}= 7.60, R_{exp}= 4.54 and χ^2 = 1.67

Table 2. Atomic coordinates, sites, occupancy factors (O.F.) and isotropic displacement parameters for Tm^{3+}, Li^{+}:$ZnWO_4$.

Atoms	*x*	*y*	*z*	O.F.	B_{iso}, Å^2	Wyckoff	Symmetry
Zn|Tm|Li	1/2	0.6828(8)	1/4	1	0.163(8)	2*f*	2
W	0	0.1857(1)	1/4	1	0.22 (0)	2*e*	2
O1	0.2675(8)	0.3765(6)	0.4075(6)	1	0.45(0)	4*g*	1
O2	0.2171(0)	0.8893(3)	0.4360(0)	1	0.36(0)	4*g*	1

The substitution of Zn^{2+} cations by Tm^{3+} ions in the $ZnWO_4$ crystal structure is expected. There is a single crystallographic site for Zn^{2+} (Wyckoff: 2*e*, C_2 symmetry). Zn^{2+} cations are reside in [ZnO_6] octahedra, displaying VI-fold oxygen coordination. This heterovalent substitution requires maintaining of the crystal electroneutrality, typically achieved through the introduction of charge compensators, e.g., univalent alkali metal cations (Na^+ or Li^+). Without such elements, vacancies at the zinc sites [11] serve as a means of charge compensation, but this leads to several detrimental effects, such as weakening of the crystal lattice and diminishing its mechanical strength characteristics, and a multi-site behavior. The ionic radii of Li^+ and Na^+ are 0.76 Å and 1.02 Å, respectively. Thus, it is expected that the former ones will more easily enter the $ZnWO_4$ lattice.

The fractional atomic coordinates (*x*, *y*, *z*), the site occupancy factors (O.F.), and the isotropic displacement parameters B_{iso} derived from the Rietveld refinement are listed in Table 2. The structure of Tm^{3+},Li^{+}:$ZnWO_4$ is shown in Fig. 3, based on the atomic coordinates determined by the Rietveld refinement. The metal-to-oxygen interatomic distances within the [WO_6] and [MO_6] (M = Zn|Tm|Li) polyhedra are detailed in Table 3. The W^{6+} ions exhibit bonding with six oxygen ions (O^{2-}), constructing distorted [WO_6] octahedra. Similarly, the Zn^{2+}|Yb^{3+}|Li^+ ions form [MO_6]

octahedra through bonding with six oxygens. These [MO_6] octahedra share corners with eight [WO_6] octahedra and edges with two [MO_6] ones. Regarding the bond lengths, for both [WO_6] and [MO_6] octahedra, there are two sets of shorter lengths measuring 1.831 Å and 2.008 Å, two intermediate lengths of 1.913 Å and 2.029 Å, and two longer ones of 2.176 Å and 2.211 Å, respectively, see Fig. 4.

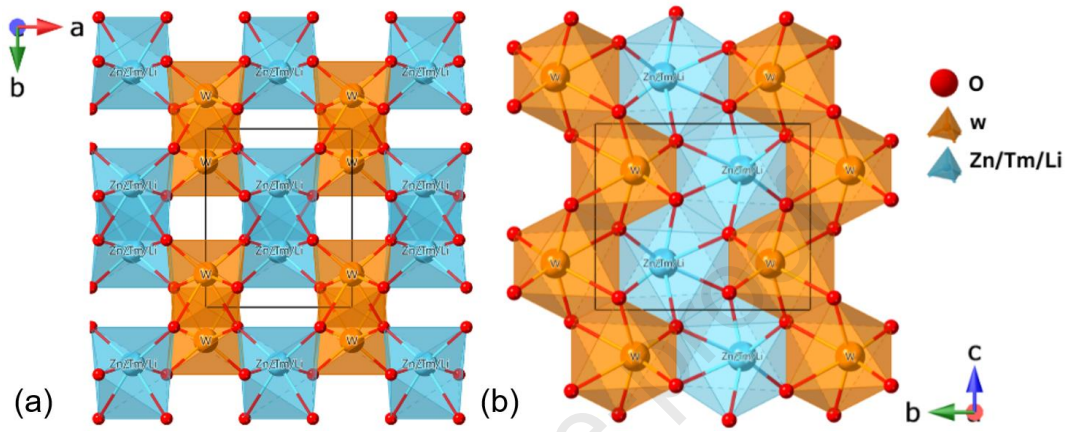

Figure 3. The structure of Tm^{3+},Li^{+}:$ZnWO_4$: (a) projection on the ***a*-*b*** plane; (b) projection on the ***b*-*c*** plane; *black lines* – unit-cell.

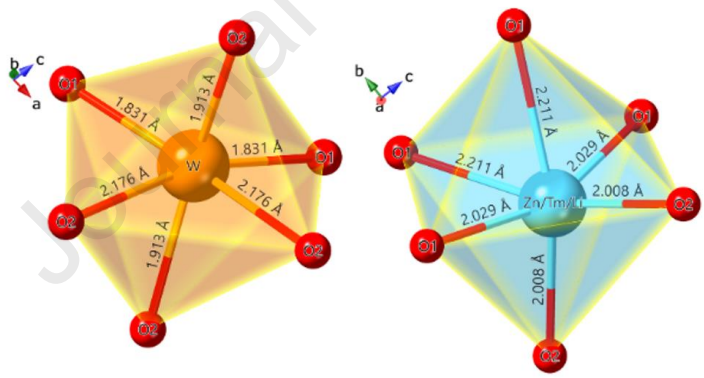

Figure 4. The coordination environment of [WO_6] and [(Zn|Tm|Li)O_6] polyhedra in $ZnWO_4$.

Table 3. Metal-oxygen distances within [WO_6] and [(Zn|Tm|Li)O_6] polyhedra in Tm^{3+},Li^{+}:$ZnWO_4$.

Polyhedron	[WO_6]	[(Zn|Tm|Li)O_6]
Interatomic distances	W-O_1 = 1.831×2	Zn|Tm|Li - O_1 = 2.029×2
M – O, Å	W-O_2 = 1.913×2	Zn|Tm|Li - O_1 = 2.211×2
	W-O_2 = 2.176×2	Zn|Tm|Li - O_2 = 2.008×2
Average bond length, Å	1.973	2.082
Polyhedron volume, $Å^3$	9.763	11.613

4. Spectroscopic characterization

$ZnWO_4$ crystallizes in the monoclinic class, and it is optically biaxial. Its optical properties are described within the optical indicatrix frame, featuring three mutually orthogonal principal axes denoted as N_p, N_m, and N_g following the notation for the principal refractive indices $n_p < n_m < n_g$. One of them (N_p) is parallel to the crystallographic ***b***-axis, aligned with the 2-fold symmetry axis. The other two axes of the optical indicatrix, N_m and N_g, lie in the ***a***-***c*** plane. The orientation of the optical indicatrix with respect to the crystallographic frame is quantified by the angles $\boldsymbol{a} \wedge N_m = 11.7°$ and $\boldsymbol{c} \wedge N_g = 12.4°$ at the wavelength of 1 μm [5], Fig. 5. The spectral measurements were performed for the principal light polarizations $\boldsymbol{E} \parallel N_p$, N_m, and N_g.

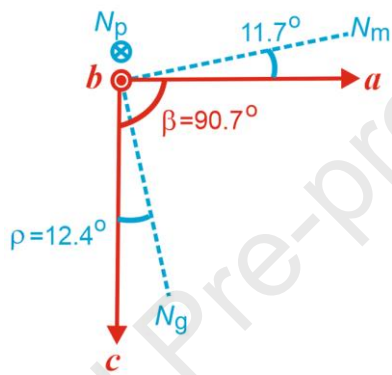

Figure 5. Orientation of the optical indicatrix axes (N_p, N_m, N_g) with respect to the crystallographic frame (***a***, ***b***, ***c***) in monoclinic $ZnWO_4$.

4.1 Raman spectroscopy

The Raman spectra were measured using a confocal μ-Raman microscope (Renishaw inVia) equipped with a ×50 Leica objective, an edge filter, and a 514-nm Ar^+ ion laser. The Porto's notations for polarized Raman spectroscopy were used, $m(nk)\bar{l}$, where m and l denote the directions of light propagation for the excitation and scattered light, respectively, and n and k represent the corresponding polarization states. The three principal crystal cuts along the N_p, N_m and N_g axes were studied, as shown in Fig. 6.

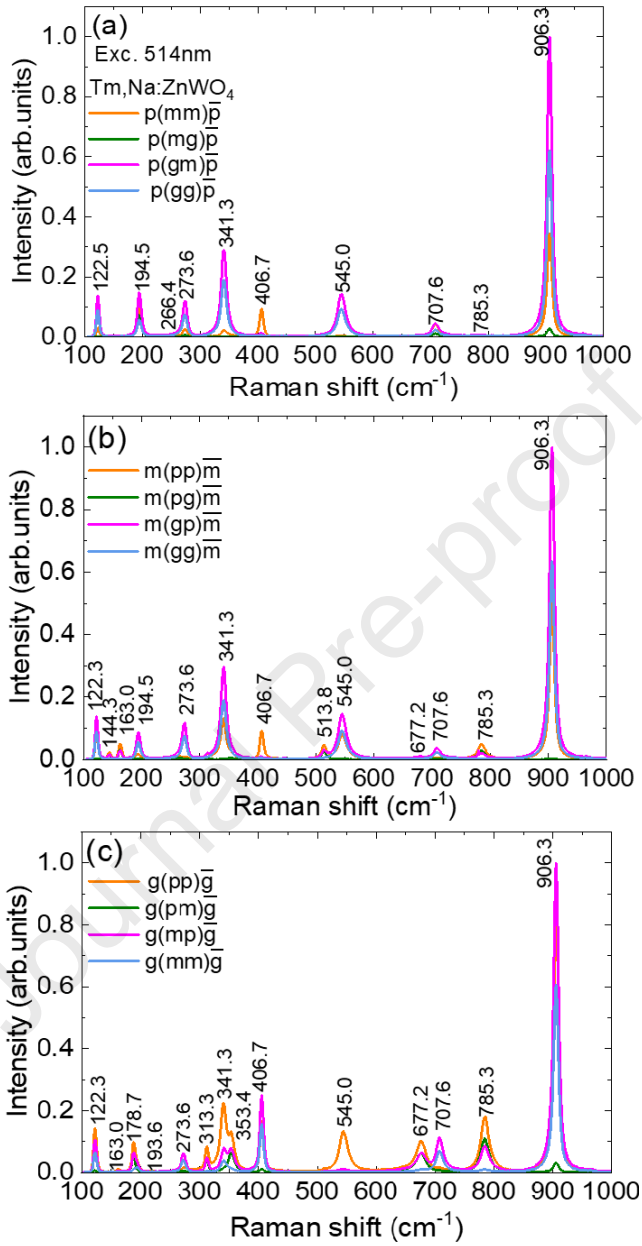

Figure 6. Polarized Raman spectra of the Tm^{3+},Na^{+}:$ZnWO_4$ crystal for the (a) $p(..)\bar{p}$, (b) $m(..)\bar{m}$, and (c) $g(..)\bar{g}$ geometries (Porto's notations). The *numbers* indicate the frequencies of Raman bands in cm^{-1}. λ_{exc} = 514 nm.

In the crystal structure of monoclinic $ZnWO_4$, there are two molecules per unit cell. According to the factor group theory analysis, the following set of irreducible representations is predicted at the center of the Brillouin zone: $\Gamma(\boldsymbol{k} = 0) = 8A_g + 10B_g + 8A_u + 10B_u$. The even (*gerade*) modes (A_g and B_g) are Raman-active, while the uneven (*ungerade*) ones (A_u and B_u) are IR-active. The

analysis of the polarized Raman spectra reveals 17 out of 18 possible Raman modes for the Tm^{3+},Na^{+}:$ZnWO_4$ crystal (the low-frequency mode below 100 cm^{-1} is missing due to the applied edge filter). The peak frequencies of the observed Raman modes, as well as the corresponding symmetries (A_g or B_g, after [23]) are detailed in Table 4.

Table 4. Raman modes for Tm^{3+},Na^{+}:$ZnWO_4$ and undoped $ZnWO_4$ crystals.

No.	Frequency, cm^{-1}		Symmetry	No.	Frequency, cm^{-1}		Symmetry
	Tm,Na:$ZnWO_4$	$ZnWO_4$ [25]			Tm,Na:$ZnWO_4$	$ZnWO_4$ [25]	
1	906.3	906.8	A_g	10	313.3	355.4	B_g
2	785.3	785.9	B_g	11	273.6	314.6	A_g
3	707.6	709.1	A_g	12	266.4	267.3	B_g
4	677.2	678.7	B_g	13	194.5	195.3	A_g
5	545	546.4	A_g	14	178.7	190	B_g
6	513.8	515.3	B_g	15	163	164.5	A_g
7	406.7	406.9	A_g	16	144.3	146.3	B_g
8	353.4	355.4	B_g	17	122.3	123.2	A_g
9	341.3	341.8	A_g	18	-	91.5	B_g

For all three principal crystal cuts, the most intense Raman band corresponds to the highest frequency vibrations, located at 906.3 cm^{-1}. Its full width at half maximum (FWHM), denoted as $\Delta\nu$, is measured to be 10.1 cm^{-1}. This band is attributed to symmetric stretching W – O vibrations (ν_1 mode, A_{1g} symmetry) within the WO_6 octahedra. It exhibits a slight blue shift and broadening when compared to the undoped $ZnWO_4$ crystal, for which ν_1 is 906.8 cm^{-1} with a corresponding $\Delta\nu$ of 8.3 cm^{-1} (at room temperature) [25]. Tm^{3+}-doped $ZnWO_4$ presents itself as a promising candidate for self-Raman frequency conversion.

4.2 Optical absorption and Judd-Ofelt analysis

The absorption spectra were measured using a Varian CARY-5000 spectrophotometer and a Glan-Taylor polarizer. The unpolarized transmission spectra of both Tm^{3+},Na^{+} and Tm^{3+},Li^{+} codoped $ZnWO_4$ crystals for the spectral range of 300 – 1100 nm are shown in Fig. 7. They are recalculated for an equal crystal thickness of 2.8 mm. For the crystal containing Na^{+} as charge compensator, even after annealing, a broad and intense absorption band related to residual color centers is observed spanning from 400 to 650 nm. Moreover, the overall transmission in the visible and near-IR spectral ranges is lower than the theoretical value determined by the Fresnel losses. The transmission of the Tm^{3+},Li^{+} codoped crystal was greatly improved as compared to the Tm^{3+},Na^{+} codoped one. Still, two broad bands around ~380 nm and 520 nm were observed in the visible indicating that the charge compensation was not complete. The UV absorption edge is at 330 nm (optical bandgap: E_g = 3.76 eV) for both crystals. The ab-initio studies of the electronic structure of $ZnWO_4$ indicated a direct bandgap of 4.65 eV [26], and the optical bandgap for undoped $ZnWO_4$ is 3.9 – 4.4 eV [27].

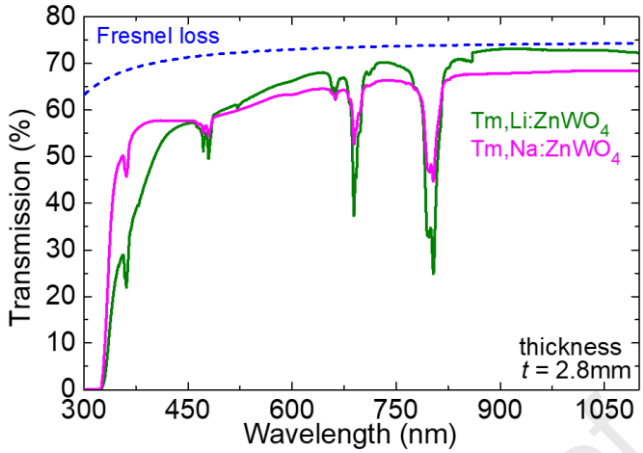

Figure 7. Unpolarized transmission spectra of Tm,Li: and Tm,Na:$ZnWO_4$ crystals recalculated for the same thickness of 2.8 mm. Non-oriented crystals.

The high sensitivity of the optical properties of $ZnWO_4$ crystals to uncontrolled impurities is well known. Even very low concentrations (1–5 ppm) of transition-metal ion impurities cause broad and strong absorption bands in these crystals around 325–350 nm, 430–450 nm and 500 nm. These bands are attributed to Fe^{3+} ions, Fe^{2+} ions and color centers at oxygen vacancies, respectively.

The polarized absorption spectra of thulium ions in the Tm^{3+},Na^{+}:$ZnWO_4$ crystal are shown in Fig. 8(a-f). The RT spectral profiles of the absorption bands were nearly identical for crystals with Na^{+} and Li^{+} charge compensators. The observed absorption bands are attributed to transitions originating from the $^3H_6$ ground state of Tm^{3+} to different excited states, namely $^3F_4$, $^3H_5$, $^3H_4$, $^3F_{2,3}$, $^1G_4$, and $^1D_2$ (in the increasing energy order). The spectra reveal strong polarization anisotropy of absorption properties.

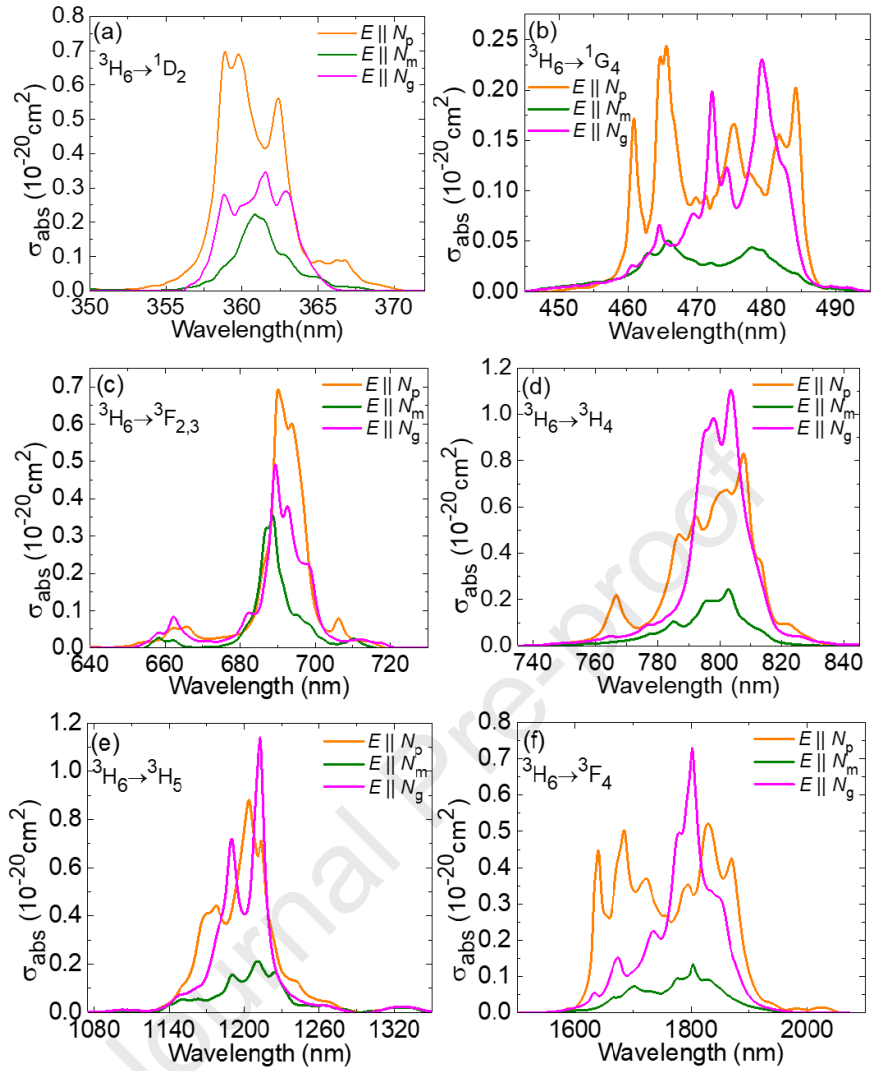

Figure 8. RT absorption cross-section, σ_{abs}, spectra of Tm^{3+} ions in the Tm^{3+},Na^+:$ZnWO_4$ crystal for transitions from the $^3H_6$ ground-state to the following excited-states: (a) $^1D_2$; (b) $^1G_4$; (c) $^3F_{2,3}$; (d) $^3G_4$; (e) $^3H_5$; and (f) $^3F_4$. The light polarizations are $\boldsymbol{E} \parallel N_p$, N_m and N_g.

The $^3H_6 \rightarrow {}^3H_4$ transition is commonly used for pumping Tm lasers, benefiting from the well-developed technology of high-power AlGaAs diode lasers emitting at 0.8 μm. Figure 8(d) depicts the polarized absorption cross-sections, derived as $\sigma_{abs} = \alpha_{abs}/N_{Tm}$, where α_{abs} is the measured absorption coefficient and N_{Tm} is the actual Tm^{3+} ion density. The maximum σ_{abs} is 1.09×10^{-20} cm^2 at 803.6 nm and the corresponding absorption bandwidth (FWHM) is 16 nm for light polarization $\boldsymbol{E} \parallel N_g$. For the other two polarization states, σ_{abs} is lower, amounting to 0.83×10^{-20} cm^2 at 807.7 nm (for $\boldsymbol{E} \parallel N_p$), and 0.24×10^{-20} cm^2 at 802.7 nm (for $\boldsymbol{E} \parallel N_m$). For the former polarization, the absorption bandwidth is superior, 25 nm. Tm^{3+} ions in $ZnWO_4$ exhibit a relatively broad absorption band around 0.8 μm. This broadening resembles that observed in Tm^{3+}-doped $MgWO_4$ (with a maximum σ_{abs} of 2.04×10^{-20} cm^2 at 802.6 nm and an absorption bandwidth of 14

nm for $\boldsymbol{E} \parallel N_g$) [18] and well exceeds the broadening for monoclinic double tungstates such as Tm:KLu$(WO_4)_2$ (σ_{abs} as high as 5.95×10^{-20} cm^2 at 802 nm however at the expense of a narrow absorption bandwidth of 4 nm for $\boldsymbol{E} \parallel N_m$) [28]. Such broadband absorption behavior significantly reduces the difficulties associated with stabilization of the emission wavelength of AlGaAs laser diodes.

The transition intensities of Tm^{3+} ions were calculated based on the measured absorption spectra using two parametrization schemes, the standard Judd-Ofelt (J-O) theory [29,30], as well as its modification accounting for a weak configuration interaction (the mJ-O theory) [31]. The J-O formalism only describes the electric dipoles (ED) contributions. The magnetic dipole (MD) transitions following the selection rule $\Delta J = J - J' = 0, \pm1$ were independently computed using the Russell–Saunders approximation on the wave functions of Tm^{3+} under the assumption of a free-ion model. The mean refractive index of $ZnWO_4$ at the average absorption / emission wavelength for each particular transition was calculated from the dispersion curves (Sellmeier equations) reported in [5].

Within the standard J-O theory, the ED line strengths S_{calc}^{ED} for $J \rightarrow J'$ transitions are:

$$S_{calc}^{ED}(JJ') = \sum_{k=2,4,6} U^{(k)}\Omega_k, \quad (1)$$

where Ω_k are the intensity (J-O) parameters and $U^{(k)}$, k = 2, 4, 6, are the squared reduced matrix elements calculated using the free-ion parameters from [32]:

$$U^{(k)} = \langle (4f^n)SLJ||U^k||(4f^n)S'L'J'\rangle^2. \quad (2)$$

In the mJ-O theory, it is postulated that only the excited configuration of the opposite parity, $4f^{n-1}5d^1$, contributes to the configuration interaction. The resulting ED line strengths are:

$$S_{calc}^{ED}(JJ') = \sum_{k=2,4,6} U^{(k)}\widetilde{\Omega}_k. \quad (3)$$

Here, the intensity parameters $\widetilde{\Omega}_k$ become linear functions of the energies (E_J and $E_{J'}$) of the two multiplets participating in the transition $J \rightarrow J'$:

$$\widetilde{\Omega}_k = \Omega_k\left[1 + 2\alpha\left(E_J + E_{J'} - 2E_f^0\right)\right], \quad (4)$$

where E_f^0 denotes the mean energy of the $4f^n$ configuration, and $\alpha \approx 1/(2\Delta)$, where $\Delta \approx E(4f^{n-1}5d^1) - E(4f^n)$ has the meaning of the average energy difference between the ground and first excited configurations. The mJ-O parametrization scheme features 4 free parameters (Ω_k, k = 2, 4, 6, and α).

Table 5 lists the experimental and calculated absorption oscillator strengths of Tm^{3+} ions in $ZnWO_4$ (f_{exp} and f_{calc}, respectively). The experimental values were polarization-averaged, $\langle f \rangle = (f_p + f_m + f_g)/3$. Two sets of f_{calc} values obtained through the J-O and mJ-O theories are given. The intensity parameters for the J-O theory are as follows: Ω_2 = 3.698, Ω_4 = 0.730 and Ω_6 = 0.405 [10^{-20} cm^2]. For the mJ-O parametrization scheme, they are Ω_2 = 5.194, Ω_4 = 0.658, Ω_6 = 0.471

[10^{-20} cm^2] and $\alpha = 0.110$ [10^{-4} cm]. The mJ-O theory was selected for derivations of the transition probabilities for two reasons. First, it yielded a lower root mean square (r.m.s.) deviation between the experimental and calculated f values (0.396 versus 0.448 for the standard J-O theory). Second, it better matched the experimental oscillator strength for the $^3H_6 \rightarrow {}^3F_4$ transition ($f_{exp} = 2.328\times10^{-6}$, cf. with f_{calc} of 2.91×10^{-6} and 2.55×10^{-6} for J-O and mJ-O theories, respectively). This oscillator strength affects the values of the radiative lifetime of the $^3F_4$ level which is the upper laser level for the 2 μm laser transition of Tm^{3+}.

Table 5. Measured and calculated absorption oscillator strengths[a] of Tm^{3+} ions in $ZnWO_4$.

Transition $^3H_6 \rightarrow {}^{2S+1}L_J$	<E>, cm^{-1}	Γ, cm^{-1}nm	f_{exp}, 10^{-6}	$U^{(2)}$	$U^{(4)}$	$U^{(6)}$	f_{calc}, 10^{-6} J-O	f_{calc}, 10^{-6} mJ-O
$^3F_4$	5762	112.3	2.33	0.5374	0.7259	0.2382	2.91^{ED}	2.55^{ED}
$^3H_5$	8393	55.48	2.54	0.1074	0.2314	0.6384	1.34^{ED}+ 0.61^{MD}	1.21^{ED}+ 0.61^{MD}
$^3H_4$	12691	32.33	3.33	0.2373	0.1090	0.5946	3.00^{ED}	3.29^{ED}
$^3F_3$+ $^3F_2$	14666	11.59	1.60	0 0	0.3163 0	0.8411 0.2580	1.94^{ED}	1.81^{ED}
$^1G_4$	21100	4.42	1.29	0.0483	0.0749	0.0125	1.06^{ED}	1.39^{ED}
$^1D_2$	27729	3.69	1.86	0	0.3156	0.0928	1.66^{ED}	1.81^{ED}
r.m.s. dev.							0.448	0.396

[a]<E> - barycenter energy of absorption band, Γ – integrated absorption coefficient, $U^{(k)}$, k = 2, 4, 6, - squared reduced matrix elements, f_{exp} and f_{calc} – experimental (polarization-averaged) and calculated absorption oscillator strengths, ED and MD – electric and magnetic dipole, respectively.

Utilizing the mJ-O theory, we calculated the probabilities of spontaneous radiative transitions ($A_{JJ'}$), the luminescence branching ratios ($B_{JJ'}$), and the radiative lifetimes (τ_{rad}) of Tm^{3+} excited states, from $^3F_4$ to $^1D_2$, see Table 6. For the $^3F_4$ state which is the upper level of the ~2 μm laser transition of Tm^{3+} ions, the radiative lifetime is 2.589 ms.

Table 6. Calculated probabilities of spontaneous radiative transitions[a] of Tm^{3+} ions in $ZnWO_4$ crystal (obtained from the mJ-O theory).

Initial state	Final state	<λ>, nm	$U^{(2)}$	$U^{(4)}$	$U^{(6)}$	$A_{JJ'}$, s^{-1}	$B_{JJ'}$, %	A_{tot}, s^{-1}	τ_{rad}, ms
$^3F_4$	$^3H_6$	1736	0.5374	0.7259	0.2382	386.1^{ED}	1	386.1	2.59
$^3H_5$	$^3F_4$	3802	0.0913	0.1279	0.9278	11.3^{ED}+0.04^{MD}	2.4	488.6	2.05
	$^3H_6$	1192	0.1074	0.2314	0.6384	316.8^{ED}+160.2^{MD}	97.6		
$^3H_4$	$^3H_5$	2326	0.0131	0.4786	0.0093	27.5^{ED}+15.8^{MD}	1.5	2795.4	0.358
	$^3F_4$	1443	0.1292	0.1301	0.2055	239.3^{ED}+40.1^{MD}	10		
	$^3H_6$	788	0.2373	0.1090	0.5946	2472.7^{ED}	88.5		

$^3F_3$,$^3F_2$	$^3H_4$	5063	0.0820 0.2965	0.3535 0.1721	0.2850 0.0792	$54.2^{ED}+0.5^{MD}$	0.4	6001.7	0.167
	$^3H_5$	1594	0.6285 0	0.3468 0.2915	0 0.5875	1092.6^{ED}	12		
	$^3F_4$	1123	0.0025 0.2994	0.0005 0.0579	0.1707 0.0430	$2273.7^{ED}+103.2^{MD}$	18.2		
	$^3H_6$	682	0 0	0.3163 0	0.8411 0.2580	2477.4^{ED}	69.4		
$^1G_4$	$^3F_2$+ $^3F_3$	1554	0.0064 0.0101	0.0719 0.0712	0.0408 0.3000	$114.1^{ED}+6.6^{MD}$	2	5884	0.170
	$^3H_4$	1189	0.1563	0.0040	0.3695	$670.5^{ED}+55.0^{MD}$	12.3		
	$^3H_5$	787	0.0727	0.0054	0.5357	$1434.7^{ED}+228.7^{MD}$	28.3		
	$^3F_4$	652	0.0035	0.0196	0.0722	$256.2^{ED}+19.4^{MD}$	4.7		
	$^3H_6$	474	0.0483	0.0749	0.0125	3098.7^{ED}	52.7		
$^1D_2$	$^1G_4$	1509	0.1844	0.1706	0.0009	803.2^{ED}	0.7	110766	0.009
	$^3F_2$+ $^3F_3$	766	0.0641 0.1646	0.3095 0.0719	0 0	$8025.8^{ED}+272.4^{MD}$	7.5		
	$^3H_4$	665	0.1274	0.0117	0.2277	6492.8^{ED}	5.9		
	$^3H_5$	517	0	0.0017	0.0163	157.6^{ED}	0.1		
	$^3F_4$	455	0.5750	0.0960	0.0226	81667^{ED}	73.7		
	$^3H_6$	361	0	0.3156	0.0928	13347^{ED}	12		

[a] $\langle\lambda\rangle$ - mean emission wavelength, $U^{(k)}$, k = 2, 4, 6, - squared reduced matrix elements, $A_{JJ'}$ – probability of spontaneous radiative transition, $B_{JJ'}$ – luminescence branching ratio, A_{tot} and τ_{rad} – total probability of spontaneous transitions and radiative lifetime of an excited-state, respectively, ED and MD – electric and magnetic dipole, respectively.

4.3 Luminescence (spectra and lifetime)

The polarized RT luminescence spectra were measured using a home-made setup comprising a CW Ti:Sapphire laser tuned to 804 nm as an excitation source, a Glan-Taylor polarizer, a CaF_2 lens, a long-pass filter (LP1400, Thorlabs), a large mode area ZrF_4 fiber for light collection and an optical spectrum analyzer (AQ6375B, Yokogawa), calibrated with a 20 W quartz lamp with a known spectral response.

The stimulated-emission (SE) cross-sections, σ_{SE}, for the $^3F_4 \rightarrow {}^3H_6$ transition around 2 μm were calculated using two approaches. First, the Füchtbauer–Ladenburg (F-L) formula was employed based on the measured polarized luminescence spectra $W_i(\lambda)$ [33]:

$$\sigma_{SE}^{i}(\lambda) = \frac{\lambda^5}{8\pi\langle n\rangle^2\tau_{rad}c}\frac{W_i(\lambda)}{1/3\sum_{j=p,m,g}\int \lambda' W_j(\lambda')d\lambda'}, \quad (5)$$

here λ is the luminescence wavelength, $\langle n\rangle$ is the averaged (over polarization) refractive index at the central emission wavelength; τ_{rad} is the radiative lifetime of the $^3F_4$ Tm^{3+} state, c is the speed of light, and the indices i and $j = p, m, g$ indicate the polarization state.

In addition, we used the reciprocity method (RM) [34]:

$$\sigma_{SE}^{i}(\lambda) = \sigma_{abs}^{i}(\lambda)\frac{Z_1}{Z_2} exp\left(-\frac{hc/\lambda - E_{ZPL}}{kT}\right), \quad (6)$$

where σ_{abs}^{i} is the absorption cross-section for the *i*-th polarization, *h* is the Planck constant, *k* is the Boltzmann constant, *T* is the crystal temperature (RT), E_{ZPL} is the energy difference between the lowest Stark sub-levels of the two multiplets (zero phonon line, ZPL), and Z_m are the partition functions of the lower (m = 1) and upper (m = 2) manifolds.

The SE cross-sections calculated by the two methods (the F-L formula and RM) agreed with each other, considering the effect of reabsorption on the measured luminescence spectra. This yielded an estimate for the radiative lifetime of the $^3F_4$ Tm^{3+} state of 2.5±0.3 ms, well in line with the calculation by the mJ-O method. The results on the σ_{SE} spectra combining these two calculation methods are shown in Fig. 9(a).

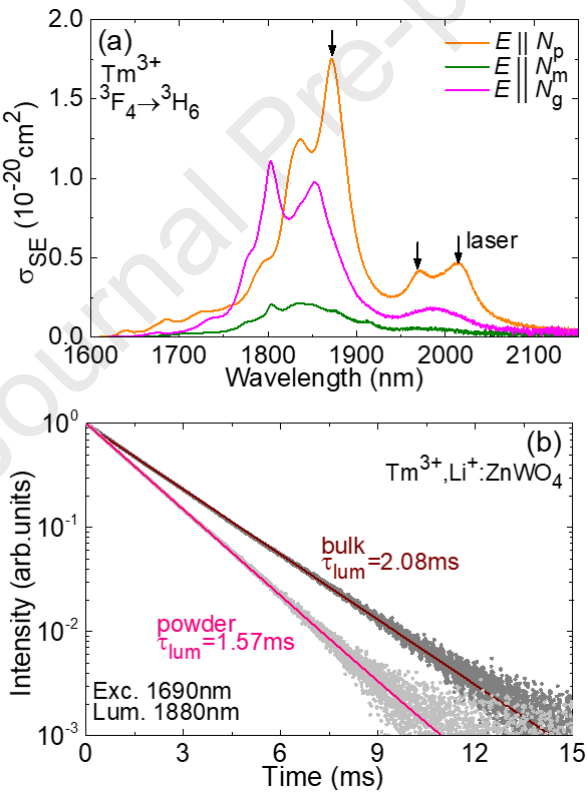

Figure 9. Emission properties of Tm,Li:$ZnWO_4$: (a) stimulated-emission (SE) cross-sections, σ_{SE}, for the $^3F_4 \rightarrow {}^3H_6$ transition (light polarizations: $\boldsymbol{E} \parallel N_p$, N_m and N_g), combined data obtained using the F-L formula and RM; (b) luminescence decay curves from the $^3F_4$ Tm^{3+} state (bulk and powdered samples).

The broad emission band spanning from 1.6 to 2.2 μm originates from the $^3F_4 \rightarrow {}^3H_6$ Tm^{3+} transition. Similar to optical absorption, Tm^{3+} ions in $ZnWO_4$ exhibit a significant polarization anisotropy of emission properties, a favorable characteristic for achieving linearly polarized laser output. Strong polarization anisotropy means also higher emission cross-section for a certain polarization compared to an isotropic crystal with the same radiative lifetime having in mind the fundamental relationship between these quantities. The maximum σ_{SE} is 1.75×10^{-20} cm^2 at 1871 nm for light polarization $\boldsymbol{E} \parallel N_p$. In the long-wave spectral region where laser action is expected to occur due to reabsorption from the ground-state in the quasi-three-level 2-μm Tm laser, the peak SE cross-sections are 0.47×10^{-20} cm^2 at 2015 nm and 0.42×10^{-20} cm^2 at 1971 nm, also for light polarized along the N_p-axis.

Tm^{3+} ions exhibit smooth and broad emission spectral profiles extending beyond 2 μm, positioning Tm^{3+}-doped $ZnWO_4$ as a promising candidate for generation of femtosecond pulses in this spectral range which is well detuned from the structured absorption of water vapors in the air, the effect known to be a limiting factor for femtosecond laser operation of many Tm^{3+}-doped laser crystals.

The SE cross-section for Tm^{3+}:$ZnWO_4$ at the expected laser wavelengths are lower than those reported previously for Tm:$MgWO_4$ (σ_{SE} = 0.97×10^{-20} cm^2 at 2015 nm for $\boldsymbol{E} \parallel N_m$) [18] and Tm:$KLu(WO_4)_2$ (σ_{SE} = 0.92×10^{-20} cm^2 at 1945 nm for $\boldsymbol{E} \parallel N_m$) [35], which is assigned to stronger spectral line broadening.

The investigation of luminescence decay at RT employed a nanosecond optical parametric oscillator (Horizon, Continuum), a 1/4 m monochromator (Oriel 77200), an InGaAs detector, and an 8 GHz digital oscilloscope (DSA70804B, Tektronix). To mitigate the impact of radiation trapping, the sample was ground into fine powder. Figure 9(b) shows the luminescence decay curves for the Tm^{3+},Li^+:$ZnWO_4$ crystal. The decay is well described by the single-exponential law, yielding a luminescence lifetime τ_{lum} of 1.57 ms for the powdered sample, as compared to 2.08 ms for the bulk crystal. For the Tm^{3+},Na^+-codoped crystal, the luminescence decay curve strongly deviated from the single exponential law yielding an average lifetime of only 1.04 ms, indicating a strong luminescence quenching assigned to energy migration to defects (evidenced by the strong tendency for color center formation). Still, even for the Tm^{3+},Li^+-codoped crystal, the luminescence lifetime was shorter than the radiative one calculated using the mJ-O theory, possibly revealing the effect of residual color centers. Indeed, the luminescence quantum yield (η_q) calculated as the ratio of τ_{lum} to τ_{rad}, is 60.8%. Note that the multiphonon non-radiative relaxation from the $^3F_4$ state of Tm^{3+} ions in $ZnWO_4$ is expected to be nearly negligible due to the relatively large energy gap to the lower-lying multiplet.

The expected laser wavelengths, and the gain profiles of Tm:$ZnWO_4$ can be evaluated through the analysis of the gain cross-section, σ_{gain}, spectra. The latter are calculated using the equation $\sigma_{gain} = \beta\sigma_{SE} - (1 - \beta)\sigma_{abs}$, where $\beta = N_2(^3F_4)/N_{Tm}$ is the population inversion ratio, i.e. the ratio of Tm^{3+} ions in the excited state, $N_2(^3F_4)$, to the total ion density N_{Tm}. The gain spectra for the $^3F_4 \rightarrow$

$^3H_6$ transition of Tm^{3+} ions in the $ZnWO_4$ crystal are plotted in Fig. 10 for the two high-gain light polarizations, namely $\boldsymbol{E} \parallel N_p$ and $\boldsymbol{E} \parallel N_g$.

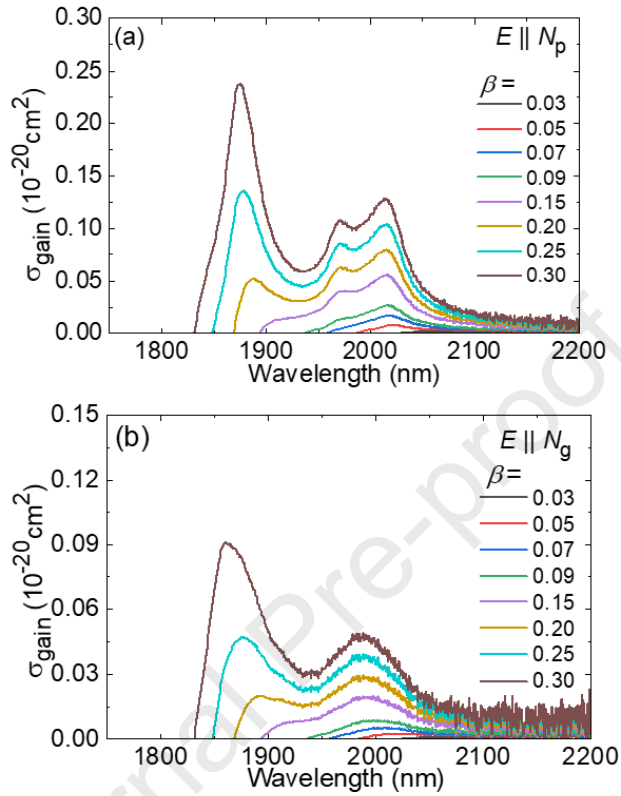

Figure 10. Gain cross-sections, $\sigma_{gain} = \beta\sigma_{SE} - (1 - \beta)\sigma_{abs}$, for the $^3F_4 \rightarrow {}^3H_6$ transition of Tm^{3+} ions in $ZnWO_4$ for light polarizations: (a) $\boldsymbol{E} \parallel N_p$ and (b) $\boldsymbol{E} \parallel N_g$. β - population inversion ratio.

For N_m-cut and N_g-cut Tm^{3+}-doped $ZnWO_4$ crystals, laser oscillations are anticipated for light polarization $\boldsymbol{E} \parallel N_p$, which corresponds to the highest gain. For this polarization state, when the inversion ratio is small ($\beta < 0.20$), the gain curves present two local peaks at 1.98 μm and 2.01 μm. For $\beta = 0.15$, the gain bandwidth (FWHM) is 83 nm. At higher inversion ratios, another intense peak appears at 1.88 μm, so that a rapid change in the laser wavelength can be expected on increasing the level of losses (e.g., output coupling) in the laser cavity. Broadband wavelength tunability across 1.8–2.1 μm is expected in this case.

4.4 Low-temperature spectroscopy and Stark splitting

With the goal of resolving the experimental crystal-field splitting for the upper ($^3F_4$) and lower ($^3H_6$) laser manifolds of the Tm^{3+} ion, we employed low-temperature (LT, 12 K) absorption and emission spectroscopy. The crystal was mounted in a cryostat (Oxford Instruments, model SU 12) with helium-gas close-cycle flow. In monoclinic $ZnWO_4$ crystals, the Tm^{3+} ions replace for the

Zn^{2+} host-forming cations in C_2 symmetry sites with a VI-fold coordination by oxygen. For this site symmetry, each $^{2S+1}L_J$ multiplet with an integer J is split into a total of $2J + 1$ Stark sub-levels. The polarized LT absorption and luminescence spectra of Tm^{3+}:$ZnWO_4$ around 2 μm (the $^3H_6 \leftrightarrow {}^3F_4$) transition are depicted in Fig. 11. The electronic transitions were assigned following the previous work on Tm^{3+}:$MgWO_4$ [6], as well as the Raman spectra of $ZnWO_4$ to eliminate the possible vibronic peaks. All Stark sub-levels of the $^3H_6$ and $^3F_4$ states were resolved. The LT absorption and emission lines of Tm^{3+} ions are broader than those in monoclinic double tungstate crystals, such as Tm:$KY(WO_4)_2$, presenting a substitutional rare-earth site, suggesting an enhanced inhomogeneous spectral line broadening probably due to the charge compensation mechanism. In our recent study of Yb^{3+}-doped $ZnWO_4$ crystals with and without Li^+, it was concluded that Li^+ codoping reduced the variety of spectroscopic sites for the rare-earth dopant resulting in a formation of a single "quasi-center" but provides a notable inhomogeneous line broadening [36]. Note that at RT, the latter effect is dominated by the homogeneous temperature broadening.

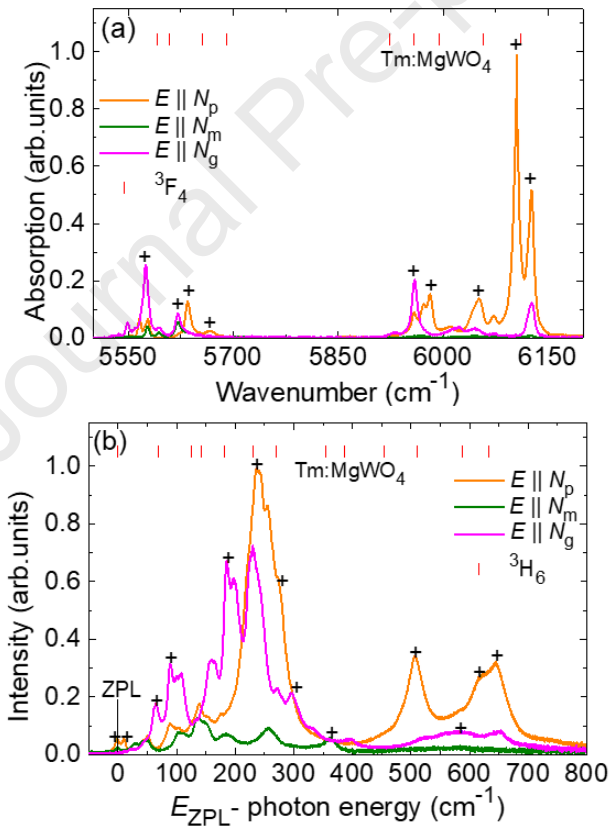

Figure 11. Low-temperature (LT, 12 K) absorption and emission spectra of Tm^{3+}:$ZnWO_4$ near 2 μm: (a) absorption, the $^3H_6 \rightarrow {}^3F_4$ transition; (b) luminescence, the $^3F_4 \rightarrow {}^3H_6$ transition. The symbol "+" marks the assigned electronic transitions. *Vertical dashes* – crystal-field splitting in Tm:$ZnWO_4$ after [6].

Figure 12 illustrates the determined experimental crystal-field splitting of the $^3H_6$ and $^3F_4$ Tm^{3+} multiplets in $ZnWO_4$. The zero-phonon line (ZPL) representing the transition between the lowest Stark sub-levels of both multiplets is found at 1794 nm (E_{ZPL} = 5574 cm^{-1}). At RT, the calculated partition functions for the ground-state and the excited-state are Z_1 = 4.922 and Z_2 = 3.695, respectively, resulting in a ratio of Z_1/Z_2 = 1.332.

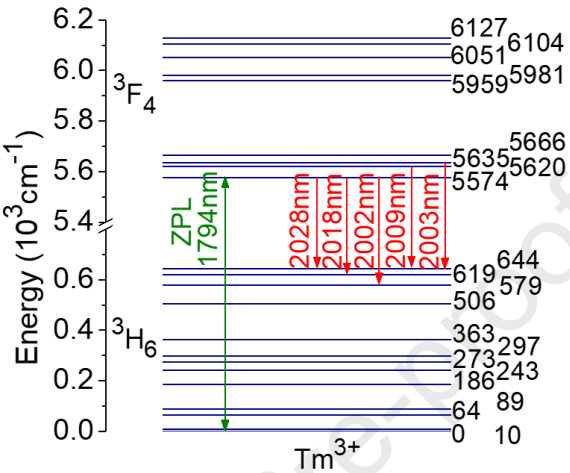

Figure 12. Experimental Stark splitting of the $^3F_4$ and $^3H_6$ Tm^{3+} multiplets in $ZnWO_4$ showing transitions responsible for emission above 2 μm, ZPL – zero-phonon line.

The Tm:$ZnWO_4$ crystal exhibits a relatively large total Stark splitting of the Tm^{3+} ground state, $\Delta E(^3H_6)$ of 644 cm^{-1}, evidencing a relatively strong crystal-field for this material. This leads to the longest wavelength of a purely electronic transition $^3F_4 \rightarrow {}^3H_6$ of 2028 nm, i.e., above 2 μm, which is rarely observed for commonly used laser host crystals. This value is higher than that previously reported for another monoclinic monotungstate crystal, Tm:$MgWO_4$ (633 cm^{-1}) [6] and well exceeds the values found for double tungstates, such as monoclinic Tm:$KLu(WO_4)_2$ (530 cm^{-1}) [37] and tetragonal Tm:$NaGd(WO_4)_2$ (373 cm^{-1}) [38]. The relatively large total Stark splitting of the ground-state of Tm^{3+} ions in $ZnWO_4$ is favorable for operation at longer wavelengths exceeding 2 μm and reducing reabsorption at the laser wavelength potentially leading to low-threshold laser operation.

5. Laser operation at 2 μm

The layout of the laser set-up is depicted in Fig. 13. Until now we were able to achieve lasing only with Tm^{3+},Li^+:$ZnWO_4$. The laser element was cut from the annealed crystal for light propagation along the N_g optical indicatrix axis (N_g-cut). It had an aperture of 7×10 mm^2 and a thickness of 2.8 mm. The crystal was polished from both sides to laser grade quality and left uncoated. The laser element was glued to a passively cooled Cu-holder using a silver paint for better heat removal. A hemispherical laser cavity comprised a plane pump mirror (PM) providing high transmission (HT) at the pump wavelength (T = 93.1% at 0.80 μm) and high reflection (HR, R >

99.9%) at 1.86 – 2.31 μm and a set of concave output couplers (OCs) having a radius of curvature (RoC) of –100 mm and a transmission at the laser wavelength T_{OC} in the range of 0.5% to 10%. The crystal was placed close to the pump mirror with an air gap of ~1 mm. The geometrical cavity length was 99 mm. The pump source was a continuous-wave Ti:Sapphire laser (3900S, Spectra Physics) delivering up to 3.6 W at ~804 nm with a nearly diffraction limited beam ($M^2 \approx 1$). The pump polarization was defined by a polarizer to correspond to $\boldsymbol{E} \parallel N_p$ in the crystal for maximized absorption via the $^3H_6 \rightarrow {}^3H_4$ transition, Fig. 8(d). The pump power was varied using an antireflection (AR) coated half-wave plate in front of the polarizer. The pump beam was first expanded using a telescope (reimaging ratio: 1:2) and then focused into the crystal through the dichroic PM by an AR-coated achromatic lens with a focal length f of 75 mm. The measured pump spot diameter in the focus was 70 ± 10 μm. The crystal was pumped in single pass. The measured pump absorption under lasing conditions decreased from 70.8% to 64.1% on increasing the output coupling due to the ground-state bleaching. We employed a long-pass filter (FEL1000, Thorlabs) to filter out the residual pump. The spectra of laser emission were measured using an optical spectrum analyzer (AQ6376, Yokogawa) and a ZrF_4 fiber.

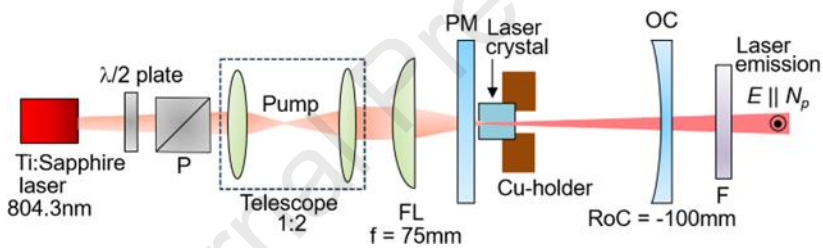

Figure 13. Scheme of the Tm^{3+},Li^+:$ZnWO_4$ laser pumped by a Ti-Sapphire laser: λ/2 - half-wave plate, P - Glan-Taylor polarizer, FL - focusing lens, PM - pump mirror, OC - output coupler, F – long pass filter.

The continuous-wave Tm^{3+},Li^+:$ZnWO_4$ laser generated a maximum output power of 282 mW at 1964-1983 nm (exhibiting a broad laser spectrum) with a slope efficiency η of 14.7% with respect the absorbed power and a laser threshold of 188 mW (when using 5% OC), Fig. 14(a). A slightly higher slope efficiency of 15.1% was achieved for higher output coupling of 10%. The laser threshold increased from 65 mW to 237 mW upon increasing the output coupling from 0.5% to 10%. The input-output dependences were linear, and neither signs of thermal effects nor thermal fracture were observed. Further scaling of the output power was limited by the available pump power. The moderate slope efficiency of the Tm^{3+},Li^+:$ZnWO_4$ laser is assigned to residual losses due to color centers which are not fully removed by the crystal annealing. The round-trip passive losses estimated using the Findlay-Clay analysis were L = 3.7%.

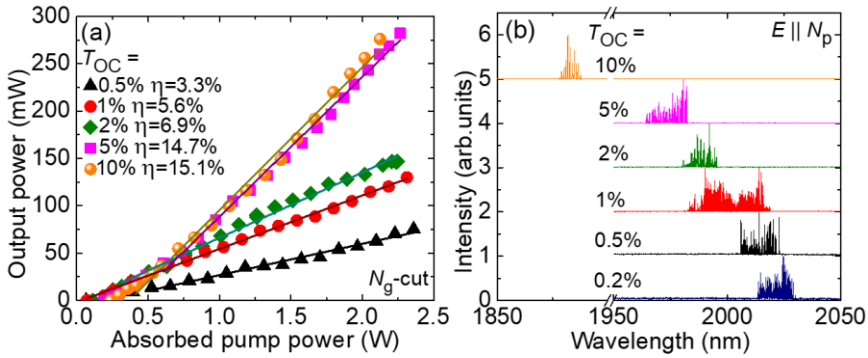

Figure 14. CW Tm^{3+},Li^+:$ZnWO_4$ laser: (a) input-output dependences, η – slope efficiency, N_g-cut crystal; (b) typical laser emission spectra, the laser polarization is $\boldsymbol{E} \parallel N_p$.

The typical spectra of laser emission measured well above the laser threshold are shown in Fig. 14(b). For small output coupling (small inversion in the gain medium), the laser operated above 2 μm, specifically in the wavelength ranges of 1982-2020 nm for 1% OC, 2006-2023 nm for 0.5% OC, and 2013-2030 nm for 0.2% OC (for the last one, the output dependence is not shown in Fig. 14(a)). This range is particularly attractive for potential applications of Tm^{3+}-doped $ZnWO_4$ crystals in mode-locked lasers due to the minimum overlap with the structured water vapor absorption lines in the air. As the output coupling increased, a continuous blue-shift of the laser wavelength was observed, leading to emission at 1878-1887 nm for the highest 10% OC. The laser spectra were relatively broad due to the smooth and structureless gain profiles of Tm:$ZnWO_4$. The laser emission was linearly polarized, and the polarization state ($\boldsymbol{E} \parallel N_p$) was naturally selected by the anisotropy of the gain of the biaxial Tm:$ZnWO_4$ crystal in agreement with Fig. 10.

6. Conclusion

To conclude, monoclinic Tm^{3+},Li^+ codoped $ZnWO_4$ crystals are attractive for ultrafast lasers emitting above 2 μm thus avoiding the structured water vapor absorption in the air, owing to a combination of attractive spectroscopic properties, namely i) broad absorption around 0.8 μm enabling efficient diode pumping, ii) broad and strongly polarized emission bands related to the $^3F_4 \rightarrow {}^3H_6$ Tm^{3+} transition supporting linear laser polarization (stimulated-emission cross-section: $\sigma_{SE} = 0.47\times10^{-20}$ cm^2 at 2015 nm for light polarization $\boldsymbol{E} \parallel N_p$), iii) a large total Stark splitting of the ground-state ($\Delta E(^3H_6) = 644$ cm^{-1}) being record-high among other mono- and double tungstate crystals responsible of emission beyond 2 μm, as well as iv) a relatively long luminescence lifetime (1.57 ms). This is coupled with the possibility to grow $ZnWO_4$ crystals by the Czochralski method (contrary to other commonly used monoclinic tungstate laser crystals grown from the flux), as well as good thermo-mechanical properties of this compound.

The feature of the present work is a direct comparison of two Tm^{3+}-doped $ZnWO_4$ crystals codoped with different univalent alkali metal cations (Na^+ or Li^+ serving for local charge

compensation). We show that Li^+ codoping is more favorable (driven by the relative closeness of ionic radii of Tm^{3+}, Li^+ and Zn^{2+}), especially in the case of optimized Tm/Li ratio, as it enables i) better optical quality of the single-crystals, ii) higher segregation coefficient for the laser-active Tm^{3+} ions (K_{Tm} = 0.40), and iii) weaker luminescence quenching for the $^3F_4$ Tm^{3+} metastable level. Altogether, this plays a key role in achieving low-threshold laser operation of Tm,Li:$ZnWO_4$ crystals around 2 μm.

From the material point of view, further progress in laser development with Tm,Li:$ZnWO_4$ should focus on increasing the actual Tm^{3+} doping level in these crystals to benefit from the cross-relaxation process among adjacent Tm^{3+} ions boosting the pump quantum efficiency, as well optimizing the growth and annealing conditions for better crystal quality. Further power scaling is expected under pumping by high-power AlGaAs laser diodes around 800 nm.

Acknowledgements

Project PID2022-141499OB-10, funded by MICIU/AEI/10.13039/501100011033/ and by FEDER/UE; Grant PECT "Cuidem el que ens uneix", operation 4 Sensòrica, Act 4 Fotònica" PR15-020174 co-financed by the European Regional Development Fund "ERDF A way of making Europe" through the ERDF Catalonia Operational Programme 2014-2020; National Natural Science Foundation of China (52072351).

References

[1] P.F. Schofield, K.S. Knight, G. Cressey, Neutron powder diffraction study of the scintillator material $ZnWO_4$, J. Mater. Sci. 31 (1996) 2873–2877. https://doi.org/10.1007/ BF00355995.

[2] X. Ren, J. Xie, S. Ruan, X. Wang, J. Pei, L. Yu, H. Yu, H. Zhang, Q. Lv, L. Guo, H. Cao, S. Xie, Y. Gao, B. He, C. Du, Diode-end-pumped solid state $ZnWO_4$ Raman laser at 2254 nm, Laser Phys. 30 (2019) 015001. https://doi.org/10.1088/1555-6611/ab4f67.

[3] X. Wang, Z. Fan, H. Yu, H. Zhang, J. Wang, Characterization of $ZnWO_4$ Raman crystal, Opt. Mater. Express 7 (2017) 1732–1744. https://doi.org/10.1364/OME.7.001732.

[4] P. Loiko, M. Chen, J.M. Serres, M. Aguiló, F. Díaz, H. Lin, G. Zhang, L. Zhang, Z. Lin, P. Camy, S.-B. Dai, Z. Chen, Y. Zhao, L. Wang, W. Chen, U. Griebner, V. Petrov, X. Mateos, Spectroscopy and high-power laser operation of a monoclinic Yb^{3+}:$MgWO_4$ crystal, Opt. Lett. 45 (2020) 1770–1773. https://doi.org/10.1364/OL.389627.

[5] A. Volokitina, S.P. David, P. Loiko, K. Subbotin, A. Titov, D. Lis, R.M. Solé, V. Jambunathan, A. Lucianetti, T. Mocek, P. Camy, W. Chen, U. Griebner, V. Petrov, M. Aguiló, F. Díaz, X. Mateos, Monoclinic zinc monotungstate Yb^{3+},Li^+:$ZnWO_4$: Part II. Polarized spectroscopy and laser operation, J. Lumin. 231 (2021) 117811. https://doi.org/10.1016/ j.jlumin.2020.117811.

[6] P. Loiko, Y. Wang, J.M. Serres, X. Mateos, M. Aguiló, F. Díaz, L. Zhang, Z. Lin, H. Lin, G. Zhang, E. Vilejshikova, E. Dunina, A. Kornienko, L. Fomicheva, V. Petrov, U. Griebner, W. Chen, Monoclinic Tm:$MgWO_4$ crystal: Crystal-field analysis, tunable and vibronic laser demonstration, J. Alloys Compd. 763 (2018) 581–591. https://doi.org/10.1016/ j.jallcom.2018.05.237.

[7] L. Zhang, P. Loiko, J.M. Serres, E. Kifle, H. Lin, G. Zhang, E. Vilejshikova, E. Dunina, A.

Kornienko, L. Fomicheva, U. Griebner, V. Petrov, Z. Lin, W. Chen, K. Subbotin, M. Aguiló, F. Díaz, X. Mateos, Growth, spectroscopy and first laser operation of monoclinic Ho^{3+}:$MgWO_4$ crystal, J. Lumin. 213 (2019) 316–325. https://doi.org/10.1016/ j.jlumin.2019.04.035.

[8] L. Li, Y. Yu, G. Wang, L. Zhang, Z. Lin, Crystal growth, spectral properties and crystal field analysis of Cr^{3+}:$MgWO_4$, CrystEngComm. 15 (2013) 6083–6089. https://doi.org/10.1039/C3CE40483H.

[9] L. Zhang, Y. Huang, S. Sun, F. Yuan, Z. Lin, G. Wang, Thermal and spectral characterization of Cr^{3+}:$MgWO_4$—a promising tunable laser material, J. Lumin. 169 (2016) 161–164. https://doi.org/10.1016/ j.jlumin.2015.08.078.

[10] Sangeeta, S.C. Sabharwal, Role of non-stoichiometry in the cracking of oxide crystals, J. Cryst. Growth. 310 (2008) 2899–2905. https://doi.org/10.1016/j.jcrysgro.2008.01.048.

[11] K. Subbotin, P. Loiko, S. Slimi, A. Volokitina, A. Titov, D. Lis, E. Chernova, S. Kuznetsov, R.M. Solé, U. Griebner, V. Petrov, M. Aguiló, F. Díaz, P. Camy, E. Zharikov, X. Mateos, Monoclinic zinc monotungstate Yb^{3+},Li^{+}:$ZnWO_4$: Part I. Czochralski growth, structure refinement and Raman spectra, J. Lumin. 228 (2020) 117601. https://doi.org/10.1016/ j.jlumin.2020.117601.

[12] R. Targ, B.C. Steakley, J.G. Hawley, L.L. Ames, P. Forney, D. Swanson, R. Stone, R.G. Otto, V. Zarifis, P. Brockman, R.S. Calloway, S.H. Klein, P.A. Robinson, Coherent lidar airborne wind sensor II: flight-test results at 2 and 10 μm, Appl. 35 (1996) 7117–7127. https://doi.org/10.1364/AO.35.007117.

[13] P. Loiko, J.M. Serres, X. Mateos, K. Yumashev, N. Kuleshov, V. Petrov, U. Griebner, M. Aguiló, F. Díaz, In-band-pumped Ho:$KLu(WO_4)_2$ microchip laser with 84% slope efficiency, Opt. Lett. 40 (2015) 344–347. https://doi.org/10.1364/OL.40.000344.

[14] V. Petrov, Frequency down-conversion of solid-state laser sources to the mid-infrared spectral range using non-oxide nonlinear crystals, Prog. Quantum Electron. 42 (2015) 1–106. https://doi.org/10.1016/j.pquantelec.2015.04.001.

[15] P. Loiko, J.M. Serres, X. Mateos, M. Aguiló, F. Díaz, L. Zhang, Z. Lin, H. Lin, G. Zhang, K. Yumashev, V. Petrov, U. Griebner, Y. Wang, S.Y. Choi, F. Rotermund, W. Chen, Monoclinic Tm^{3+}:$MgWO_4$: a promising crystal for continuous-wave and passively Q-switched lasers at ∽2 μm, Opt. Lett. 42 (2017) 1177–1180. https://doi.org/10.1364/OL.42.001177.

[16] Y. Wang, W. Chen, M. Mero, L. Zhang, H. Lin, Z. Lin, G. Zhang, F. Rotermund, Y.J. Cho, P. Loiko, X. Mateos, U. Griebner, V. Petrov, Sub-100 fs Tm:$MgWO_4$ laser at 2017 nm mode locked by a graphene saturable absorber, Opt. Lett. 42 (2017) 3076–3079. https://doi.org/10.1364/OL.42.003076.

[17] L. Wang, W. Chen, Y. Zhao, Y. Wang, Z. Pan, H. Lin, G. Zhang, L. Zhang, Z. Lin, J.E. Bae, T.G. Park, F. Rotermund, P. Loiko, X. Mateos, M. Mero, U. Griebner, V. Petrov, Single-walled carbon-nanotube saturable absorber assisted Kerr-lens mode-locked Tm:$MgWO_4$ laser, Opt. Lett. 45 (2020) 6142–6145. https://doi.org/10.1364/OL.411288.

[18] L. Zhang, H. Lin, G. Zhang, X. Mateos, J.M. Serres, M. Aguiló, F. Díaz, U. Griebner, V. Petrov, Y. Wang, P. Loiko, E. Vilejshikova, K. Yumashev, Z. Lin, W. Chen, Crystal growth, optical spectroscopy and laser action of Tm^{3+}-doped monoclinic magnesium tungstate, Opt. Express, 25 (2017) 3682–3693. https://doi.org/10.1364/OE.25.003682.

[19] S. O'Hara, G.M. McManus, Czochralski growth of low-dislocation-density zinc tungstate

crystals, J. Appl. Phys. 36 (1965) 1741–1746. https://doi.org/10.1063/1.1703120.

[20] F. Yang, C. Tu, J. Li, G. Jia, H. Wang, Y. Wei, Z. You, Z. Zhu, Y. Wang, X. Lu, Growth and optical property of $ZnWO_4$: Er^{3+} crystal, J. Lumin. 126 (2007) 623–628. https://doi.org/10.1016/ j.jlumin.2006.10.015.

[21] F. Yang, C. Tu, H. Wang, Y. Wei, Z. You, G. Jia, J. Li, Z. Zhu, X. Lu, Y. Wang, Growth and spectroscopy of Dy^{3+} doped in $ZnWO_4$ crystal, Opt. Mater. 29 (2007) 1861–1865. https://doi.org/10.1016/ j.optmat.2006.10.014.

[22] F. Yang, C. Tu, The spectroscopy investigation of $ZnWO_4$:Tm^{3+} single crystal, J. Alloys Compd 535 (2012) 83-86, https://doi.org/10.1016/j.jallcom.2012.04.084.

[23] K.A. Subbotin, A.I. Titov, S.K. Pavlov, P.A. Volkov, V. V. Sanina, D.A. Lis, O.N. Lis, Y.I. Zimina, Y.S. Didenko, E. V. Zharikov, Effect of Li^+ codoping on the mechanical strength of Yb:$ZnWO_4$ single crystals, J. Cryst. Growth. 582 (2022) 126498. https://doi.org/10.1016/ j.jcrysgro.2021.126498.

[24] P.F. Schofield, K.S. Knight, S.A.T. Redfern, G. Cressey, Distortion characteristics across the structural phase transition in $(Cu_{1-x}Zn_x)WO_4$, Acta Cryst. 53 (1997) 102–112. https://doi.org/10.1107/S0108768196010403.

[25] H. Wang, F.D. Medina, Y.D. Zhou, Q.N. Zhang, Temperature dependence of the polarized Raman spectra of $ZnWO_4$ single crystals, Phys. Rev. B. 45 (1992) 10356. https://doi.org/10.1103/PhysRevB.45.10356.

[26] M.G. Brik, V. Nagirnyi, M. Kirm, Ab-initio studies of the electronic and optical properties of $ZnWO_4$ and $CdWO_4$ single crystals, Mater. Chem. Phys. 134 (2012) 1113–1120. https://doi.org/10.1016/ j.matchemphys.2012.04.003.

[27] R. Lacomba-Perales, J. Ruiz-Fuertes, D. Errandonea, D. Martínez-García, A. Segura, Optical absorption of divalent metal tungstates: Correlation between the band-gap energy and the cation ionic radius, Europhys. Lett. 83 (2008) 37002. https://doi.org/10.1209/0295-5075/83/37002.

[28] V. Petrov, J. Liu, M. Galan, G. Viera, C. Pujol, U. Griebner, M. Aguilo, F. Diaz, Efficient diode-pumped cw Tm:$KLu(WO_4)_2$ laser, Proc. SPIE 6216 (2006) https://doi.org/10.1117/12.665457.

[29] G.S. Ofelt, Intensities of crystal spectra of rare-earth ions, J. Chem. Phys. 37 (1962) 511–520. https://doi.org/10.1063/1.1701366.

[30] B.R. Judd, Optical absorption intensities of rare-earth ions, Phys. Rev. 127 (1962) 750-761. https://doi.org/10.1103/PhysRev.127.750.

[31] P. Loiko, A. Volokitina, X. Mateos, E. Dunina, A. Kornienko, E. Vilejshikova, M. Aguiló, F. Díaz, Spectroscopy of Tb^{3+} ions in monoclinic $KLu(WO_4)_2$ crystal application of an intermediate configuration interaction theory, Opt. Mater. 78 (2018) 495–501. https://doi.org/10.1016/ j.optmat.2018.03.014.

[32] W.T. Carnall, P.R. Fields, K. Rajnak, Electronic energy levels in the trivalent lanthanide aquo ions. I. Pr^{3+}, Nd^{3+}, Pm^{3+}, Sm^{3+}, Dy^{3+}, Ho^{3+}, Er^{3+}, and Tm^{3+}, J. Chem. Phys. 49 (1968) 4424–4442. https://doi.org/10.1063/1.1669893.

[33] B.F. Aull, H.P. Jenssen, Vibronic Interactions in Nd:YAG resulting in nonreciprocity of absorption and stimulated emission cross sections, IEEE J. Quantum Electron. 18 (1982) 925–930. https://doi.org/10.1109/JQE.1982.1071611.

[34] S.A. Payne, L.L. Chase, L.K. Smith, W.L. Kway, W.F. krupke, Infrared cross-section

measurements for crystals doped with Er^{3+}, Tm^{3+}, and Ho^{3+}, IEEE J. Quantum Electron. 28 (1992) 2619–2630. https://doi.org/10.1109/3.161321.

[35] V. Petrov, M.C. Pujol, X. Mateos, Ò. Silvestre, S. Rivier, M. Aguiló, R.M. Solé, J. Liu, U. Griebner, F. Díaz, Growth and properties of $KLu(WO_4)_2$, and novel ytterbium and thulium lasers based on this monoclinic crystalline host, Laser Photon. Rev. 1 (2007) 179–212. https://doi.org/10.1002/lpor.200710010.

[36] G.Z. Elabedine, K. Subbotin, P. Loiko, Y. Zimina, S. Pavlov, A. Titov, P. Camy, A. Braud, R.M. Solé, M. Aguiló, F. Díaz, W. Chen, X. Mateos, V. Petrov, Monoclinic Yb^{3+},Li^{+}:$ZnWO_4$ - efficient broadly emitting laser material, Proc. SPIE 12864 (2024) https://doi.org/10.1117/12.3002431.

[37] O. Silvestre, M.C. Pujol, M. Rico, F. Güell, M. Aguiló, F. Díaz, Thulium doped monoclinic $KLu(WO_4)_2$ single crystals: Growth and spectroscopy, Appl. Phys. B 87 (2007) 707–716. https://doi.org/10.1007/ s00340-007-2664-0.

[38] J.M. Cano-Torres, M. Rico, X. Han, M.D. Serrano, C. Cascales, C. Zaldo, V. Petrov, U. Griebner, X. Mateos, P. Koopmann, C. Kränkel, Comparative study of crystallographic, spectroscopic, and laser properties of Tm^{3+} in $NaT(WO_4)_2$ (T=La, Gd, Y, and Lu) disordered single crystals, Phys. Rev. B 84 (2011) 174207. https://doi.org/10.1103/ PhysRevB.84.174207.

- Czochralski growth of monoclinic Tm^{3+}, $Na^{+}(Li^{+})$ codoped zinc monotungstate ($ZnWO_4$);
- Li^{+} codoping provides higher Tm^{3+} segregation and longer luminescence lifetime;
- Tm,Li:$ZnWO_4$ features strongly polarized emission spectra extending beyond 2 μm;
- The stimulated-emission cross-section is 0.47×10^{-20} cm^2 at 2015 nm;
- First continuous-wave laser operation of Tm,Li:$ZnWO_4$ crystal at 2 μm is demonstrated.

Declaration of interests

☒ The authors declare that they have no known competing financial interests or personal relationships that could have appeared to influence the work reported in this paper.

☐ The authors declare the following financial interests/personal relationships which may be considered as potential competing interests: